

High Total Proton Conductivity in Large-Grained Yttrium-Doped Barium Zirconate

Yoshihiro Yamazaki, Raul Hernandez-Sanchez, and Sossina M Haile*

Materials Science, California Institute of Technology, 1200 California Blvd., Pasadena, California 91125

Received January 22, 2009. Revised Manuscript Received April 8, 2009

Barium zirconate has attracted particular attention among candidate proton conducting electrolyte materials for fuel cells and other electrochemical applications because of its chemical stability, mechanical robustness, and high bulk proton conductivity. Development of electrochemical devices based on this material, however, has been hampered by the high resistance of grain boundaries, and, due to limited grain growth during sintering, the high number density of such boundaries. Here, we demonstrate a fabrication protocol based on the sol–gel synthesis of nanocrystalline precursor materials and reactive sintering that results in large-grained, polycrystalline $\text{BaZr}_{0.8}\text{Y}_{0.2}\text{O}_{3-\delta}$ of total high conductivity, $\sim 1 \times 10^{-2} \text{ Scm}^{-1}$ at 450 °C. The detrimental role of grain boundaries in these materials is confirmed via a comparison of the conductivities of polycrystalline samples with different grain sizes. Specifically, two samples with grain sizes differing by a factor of 2.3 display essentially identical grain interior conductivities, whereas the total grain boundary conductivities differ by a factor of 2.5–3.2, depending on the temperature (with the larger-grained material displaying higher conductivity).

1. Introduction

The environmental benefits of fuel cells for electric power generation, including zero regulated emissions and high efficiency, have been increasingly appreciated in recent years. Of known fuel cell types, solid oxide fuel cells (SOFCs) based on proton conducting electrolytes offer the unique combination of high efficiency at high utilization of hydrogen fuel and the flexibility to readily operate on hydrocarbon or alcohol fuels.^{1–3} The former characteristic results because the wastewater is generated at the air rather than the fuel electrode, eliminating the fuel dilution effects that occur in conventional SOFCs based on oxygen ion conductors, whereas the latter results simply because of the intermediate temperature of operability (400–600 °C), at which catalyzed electro-oxidation or steam reforming of complex fuels can occur, unlike the case of polymer electrolyte membrane fuel cells. This intermediate temperature regime further alleviates materials compatibility and lifetime challenges typical of conventional high-temperature SOFCs that operate at 800–1000 °C.

Proton incorporation in trivalent-doped perovskite oxides of high proton conductivity is widely recognized to occur via a two-step process.^{3–5} On synthesis, the trivalent species, which ideally resides on the tetravalent site, is charge-compensated by oxygen vacancies. Upon

exposure to H_2O vapor, hydroxyl groups are incorporated at formerly vacant oxygen sites, and proton transport occurs via proton hopping between oxygen sites. High conductivity via such a mechanism has long been recognized in doped barium cerate⁶ and doped strontium cerate.⁷ These materials, however, have poor chemical stability in CO_2 -containing atmospheres, creating significant obstacles to their technological implementation. In contrast, barium zirconate has good chemical stability, but initial measurements suggested extremely low proton conductivity.⁸ More recent studies have shown that, in fact, the bulk (or grain interior) conductivity of doped barium zirconate is substantial, in particular when doped by yttrium,^{9–11} but that a high number density of highly resistive grain boundaries in the material leads to a total (or effective) conductivity that is unacceptably low for fuel cell and other applications.¹² Thus, the promising bulk characteristics have not materialized into technologically relevant devices.

In order to obtain barium zirconate materials with high total conductivity, one can attempt to improve the inherent transport characteristics of the grain boundaries or reduce the number density of such boundaries via

*Corresponding author. E-mail: smhaile@caltech.edu.

- (1) Steele, B. C. H.; Heinzel, A. *Nature* **2001**, 414(6861), 345–352.
- (2) Haile, S. M. *Acta Mater.* **2003**, 51(19), 5981–6000.
- (3) Kreuer, K. D. *Annu. Rev. Mater. Res.* **2003**, 33, 333–359.
- (4) Iwahara, H. *Solid State Ionics* **1996**, 86–8, 9–15.
- (5) Norby, T. *Solid State Ionics* **1999**, 125(1–4), 1–11.

- (6) Bonanos, N. *Solid State Ionics* **1992**, 53–6, 967–974.
- (7) Iwahara, H.; Uchida, H.; Tanaka, S. *Solid State Ionics* **1983**, 9–10, 1021–1025.
- (8) Iwahara, H.; Yajima, T.; Hibino, T.; Ozaki, K.; Suzuki, H. *Solid State Ionics* **1993**, 61(1–3), 65–69.
- (9) Kreuer, K. D. *Solid State Ionics* **1999**, 125(1–4), 285–302.
- (10) Bohn, H. G.; Schober, T. *J. Am. Ceram. Soc.* **2000**, 83(4), 768–772.
- (11) Kreuer, K. D.; Adams, S.; Munch, W.; Fuchs, A.; Klock, U.; Maier, J. *Solid State Ionics* **2001**, 145(1–4), 295–306.
- (12) Babilo, P.; Uda, T.; Haile, S. M. *J. Mater. Res.* **2007**, 22(5), 1322–1330.

enhanced grain growth. In pursuit of the latter, enhanced grain growth has been demonstrated in the recent literature through the use of sintering aids such as ZnO ,^{13,14} MgO , and Al_2O_3 ,¹⁵ the use of alternative dopants such as Sc_2O_3 ,¹⁶ or via extreme high-temperature treatments.¹⁷ In those cases where the influence on grain boundary conductivity has been examined, it has been observed that sintering aids that enhance grain growth unfortunately increase the resistivity of the boundaries, whereas Sc as a dopant leads to low bulk conductivity. Heat treatment at $\sim 2200^\circ\text{C}$ provides enhanced grain growth, but it is impractical for most applications, and more significantly, improved proton transport has not been obtained. Thus, none of the grain growth methods demonstrated to date have proven successful toward achieving the ultimate goal of high total conductivity as required for high-efficiency electrochemical devices.

The anticipated enormous environmental benefits of fuel cells and other devices based on doped barium zirconate motivate a search for alternative sintering strategies that yield large-grained materials with the desired transport characteristics. Here, we have pursued a strategy in which a green body is formed of precursor phases which are distinct from that of the final complex oxide. The sintering of such green bodies can proceed more effectively than more traditional methods in which phase formation is completed prior to densification. This process of simultaneous reaction and sintering, termed “reactive sintering”, may or may not involve a liquid phase and can lead to both lower sintering temperatures and enhanced grain growth.¹⁸ By way of implementation, we have prepared here nanocrystalline $\text{BaZr}_{0.8}\text{Y}_{0.2}\text{O}_{3-\delta}$ (BYZ20) using a polymeric precursor (sol–gel) route and examined the influence of incomplete calcination on microstructural characteristics and proton conductivity. It is shown that, through suitable control of the calcination step, a final sintered body with an average distance between grain boundaries of $1.00\ \mu\text{m}$ and total conductivity of $1 \times 10^{-2}\ \text{Scm}^{-1}$ at 450°C can be attained.

2. Experimental Section

The materials were synthesized via a chemical solution route in which high-purity $\text{Ba}(\text{NO}_3)_2$, $\text{Y}(\text{NO}_3)_3 \cdot 6\text{H}_2\text{O}$, and $\text{ZrO}(\text{NO}_3)_2 \cdot x\text{H}_2\text{O}$, where x was determined to be 2.24 by thermogravimetric analysis, were used as the precursor reagents and ethylene diamine tetraacetic acid (EDTA) and citric acid served as chelating agents. The molar ratio between total metal cations, EDTA acid, and citric acid was fixed at 1:1.5:1.5. After dissolution of the nitrates into deionized water, EDTA and NH_4OH were added into the solution with the NH_4OH content

adjusted to obtain a pH of ~ 9 . Citric acid was then added, and the solution pH was set at ~ 10 , again by adjustment of the NH_4OH content. The solvents were removed upon heat treatment at $\sim 100^\circ\text{C}$ for over 10 h, transforming the solution to a semirigid gel. This material calcined at selected temperatures between 850 and 1200°C for 5 h in air and gently milled at 50 rpm for a week using 3 mm zirconia media.

Phase analysis was performed by X-ray powder diffraction using a Phillips X'Pert Pro powder diffractometer ($\text{Cu K}\alpha$, 45 kV, 40 mA). The crystallite size and surface area of the powders were determined using the Scherrer equation after Rietveld refinement and Brunauer–Emmett–Teller analysis, respectively. The weight percentage of barium carbonate in the powder was also obtained from the X-ray diffractions using a calibration curve.

Dense compacts for microstructural evaluation and conductivity measurements were obtained as follows. About 10 drops of binder solution composed of 200 mL of water, 2 g of polyvinyl alcohol, 1 mL of glycerin, and 10 mL of ethanol were added to $\sim 10\ \text{g}$ of the loose powder, and the lightly milled mixture was uniaxially pressed at 45 MPa. The green body was then isostatically pressed at pressures of 300–370 MPa. The binder was removed by heat treatment at 600°C for 1 h under air and the samples subsequently sintered at 1600°C (reached using a heating rate of 5°C min^{-1}) for 24 h under flowing oxygen. To minimize the extent of possible BaO loss during high-temperature processing, samples were covered using a mixture of 90 mass % BYZ20 and 10 mass % barium carbonate during the sintering step.

The cross-sectional microstructure of the pellets was observed using LEO 1550 VP field emission scanning electron microscopy (10 kV excitation voltage; In-lens mode; Carl Zeiss) after carbon coating. The average distance between grain boundaries was determined using the mean linear intercept method. The grain size distribution of pellets was determined using the cross-sectional images and the image analysis software ImageJ (National Institute of Mental Health). More than 160 grains were used to obtain each grain boundary distribution. Quantitative elemental microanalyses were conducted with a JEOL 8200 electron probe microanalysis operated at 15 kV and 25 nA using a beam $10\ \mu\text{m}$ in diameter. The relative density of the pellets was measured by the Archimedes method using deionized water with respect to the theoretical density of undoped BaZrO_3 ($6.21\ \text{g cm}^{-3}$).

The conductivity of sintered pellets was measured by AC impedance spectroscopy under a water-saturated N_2 or Ar atmosphere ($P_{\text{H}_2\text{O}} = 0.031\ \text{atm}$) from 54 to 600°C using an equilibration time of 30 min for each temperature. The measurement sequence was repeated several times until the resistivities at each temperature became equivalent from one measurement to the next. Data were collected in the frequency range from 10^{-1} to $1.3 \times 10^7\ \text{Hz}$ using a Solartron 1260 and a voltage amplitude of 20 mV. Silver electrodes were applied onto the surfaces of polished samples by brush painting colloidal silver paint (No. 16032, Ted Pella, Inc., Redding, CA).

The resulting impedance spectra were analyzed in terms of an equivalent circuit model in which (depending on the temperature regime) distinct RQ subcircuits were used to represent the grain interior and grain boundary regions, where R is an ideal resistor with $Z_R = R$, and Q is a constant phase element with $Z_Q = (Y(j\omega)^n)^{-1}$, where j is $\sqrt{-1}$, ω is the frequency, and Y and n are constants with $0 < n < 1$. The capacitance, C , of an RQ circuit was obtained from the relation $C = Y^{1/n}R^{(1/n-1)}$. The average values of n obtained for grain interior and grain

(13) Babilo, P.; Haile, S. M. *J. Am. Ceram. Soc.* **2005**, 88(9), 2362–2368.

(14) Tao, S. W.; Irvine, J. T. S. *Adv. Mater.* **2006**, 18(12), 1581.

(15) Azad, A. M.; Subramaniam, S.; Dung, T. W. *J. Alloys Compd.* **2002**, 334, 118–130.

(16) Imashuku, S.; Uda, T.; Nose, Y.; Kishida, K.; Harada, S.; Inui, H.; Awakura, Y. *J. Electrochem. Soc.* **2008**, 155(6), B581–B586.

(17) Duval, S. B. C.; Holtappels, P.; Vogt, U. F.; Pomjakushina, E.; Conder, K.; Stimming, U.; Graule, T. *Solid State Ionics* **2007**, 178 (25–26), 1437–1441.

(18) Kwon, S.; Sabolsky, E. M. *J. Am. Ceram. Soc.* **2001**, 84(3), 648–650.

boundary subcircuits were both close to 1 (typically ~ 0.95 and ~ 0.9 , respectively), as required for meaningfully determining the capacitance by this expression. The data analysis was performed using the software package Zview (Scribner Associates Inc., Southern Pines, NC). Use of a four-wire configuration in conjunction with a Solartron 1260 permitted direct measurement of the grain interior conductivity to ~ 350 °C, a slightly higher high-temperature limit than that previously achieved in the literature (300 °C).^{10,12} Conversion from effective to specific grain boundary conductivity was achieved using eq 7, as given below, and a single, temperature-averaged value of C_{GI}/C_{GB} for each sample.

3. Results and Discussion

3.1. Precursor Materials. The X-ray powder diffraction patterns of powders calcined at temperatures between 850 and 1200 °C (Figure 1) show the precursor materials to be composed primarily of the cubic perovskite phase, with the carbonate phase (BaCO_3) occurring at lower calcination temperatures. Specifically, the weight percentage of the carbonate phase is 30% at the lowest calcination temperature (850 °C), falls gradually, and disappears entirely from the diffraction pattern only at a calcination temperature of 1200 °C, Figure 2a. Even at the highest barium carbonate quantities, the peak intensities from unidentified phases is low (too low for meaningful quantification), implying that the majority cubic perovskite must be highly deficient in barium, with as much as ~ 40 mol % of the barium sites being unoccupied in the sample calcined at 850 °C to account for a composite with 30 wt % barium carbonate. In contrast to the barium carbonate content, the crystallite size in the perovskite phase and the specific surface area of the composite powder vary nonmonotonically with the calcination temperature. The crystallite size, as evaluated by the widths of the relevant diffraction peaks, first decreases and then increases with the calcination temperature, attaining a minimum value of 12 nm for calcination at 950 °C (Figure 2b), whereas the specific surface area of the powder mixture, as determined by nitrogen sorption measurements, first increases and then decreases with increasing calcination temperature, reaching a maximum value of $28 \text{ m}^2 \text{ g}^{-1}$ around 1000 °C (Figure 2c). The conditions leading to a minimum in perovskite crystallite size correspond reasonably well to those leading to a maximum in the specific surface area.

3.2. Grain Growth of Polycrystalline Yttrium-Doped Barium Zirconate. The microstructure and grain size distribution within sintered BYZ20 pellets are presented in Figures 3 and 4, respectively (again, for powders calcined between 850 and 1200 °C). The diffraction patterns collected postsintering (not shown) indicated all samples to have converted to single-phase perovskite, irrespective of the initial barium carbonate content, suggesting that BaCO_3 decomposes and reacts with the nonstoichiometric perovskite phase during sintering (reactive sintering). The sintering conditions were identical, 1600 °C for 24 h, and hence the notable microstructural differences result directly from the differences

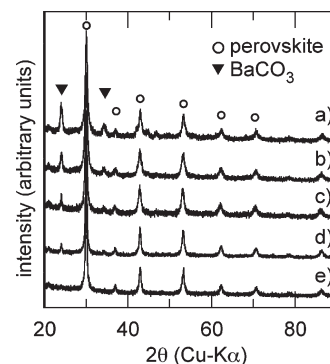


Figure 1. X-ray diffraction patterns of powders calcined at (a) 850 °C, (b) 950 °C, (c) 1050 °C, (d) 1150 °C, and (e) 1200 °C.

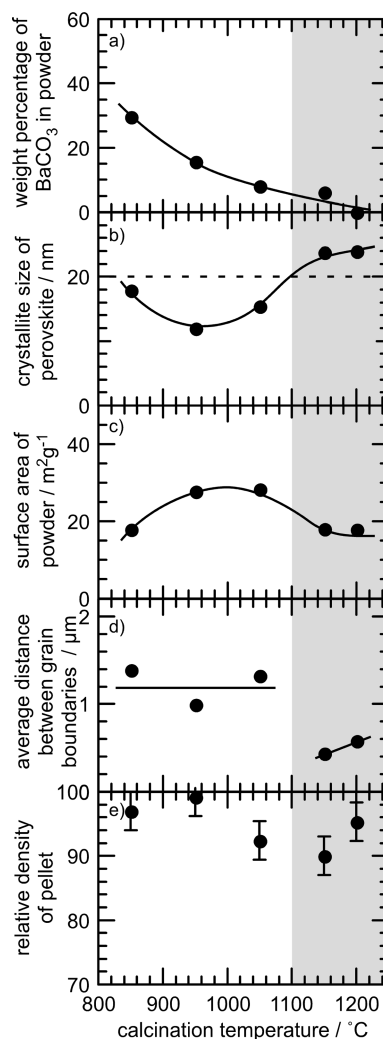


Figure 2. Plots of (a) weight percentage of barium carbonate in powder, (b) crystallite size of perovskite, (c) surface area of powder, (d) average grain-boundary distance in pellet, and (e) relative density of pellets as a function of powder calcination temperature.

in calcination temperature. Samples calcined at temperatures between 850 and 1050 °C all displayed an average distance between grain boundaries of $\sim 1.2 \mu\text{m}$, whereas those calcined at higher temperatures of 1150 and 1200 °C displayed a mean distance almost 2.5 times smaller, about $0.5 \mu\text{m}$. Furthermore, the lower-temperature calcined samples displayed a wide grain size distribution in

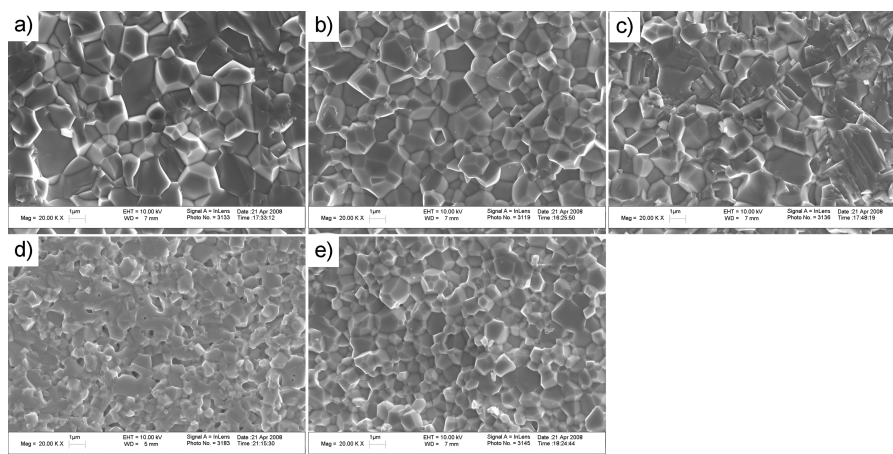


Figure 3. Cross-sectional scanning electron microscopy images of BYZ20 pellets sintered under the same conditions using powders calcined at (a) 850 °C, (b) 950 °C, (c) 1050 °C, (d) 1150 °C, and (e) 1200 °C.

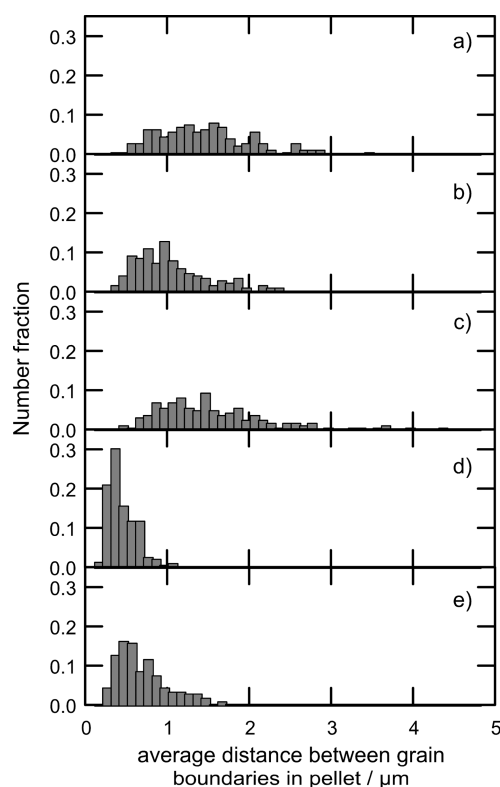


Figure 4. Grain size distribution in sintered BYZ20 pellets synthesized using powders calcined at (a) 850 °C, (b) 950 °C, (c) 1050 °C, (d) 1150 °C, and (e) 1200 °C. Samples prepared using powders calcined at temperatures lower than 1050 °C have substantially larger grains ($\sim 1.2 \mu\text{m}$) than those ($\sim 0.5 \mu\text{m}$) obtained from powder calcined at higher temperatures.

contrast to the relatively narrow grain size distribution of the higher-temperature calcined samples. Unlike the grain characteristics, the extent of densification was found to be relatively independent of calcination temperature, varying nonsystematically from 90 to 99% of theoretical, Figure 2e.

At first glance, it appears that the abrupt change in grain growth behavior can be attributed to the crystallite size in the perovskite phase, which is less than 20 nm at a calcination temperature of 1050 °C or lower. However, attempts in the literature to employ nanometric, high specific surface area powders of yttrium-doped barium

zirconate to improve sinterability, while often successful at reducing the temperatures and times required for densification, have had little impact on grain growth. For example, Cervera et al. prepared BYZ20 powders with particle sizes in the 3–5 nm range, and ultimately obtained dense compacts with grain sizes no larger than 200 nm.¹⁹ This observation suggests that the morphological features of the perovskite phase may not be entirely responsible for the enhanced grain growth that occurs in the low-temperature calcined samples. The large-grained compacts obtained here differ from the previous studies in that a substantial carbonate content was retained prior to sintering. Thus, it appears that both nanometric powders of the precursor perovskite phase and residual carbonate (the latter implying an initial barium deficiency in the perovskite phase) are required to obtain large-grained materials under moderate sintering conditions. It is relevant that a similar enhancement of grain growth has been observed in In-doped calcium zirconate when carbonate is present in the pressed compact.²⁰ In contrast to the present results, however, Sin et al. have obtained high-density, large-grained ($>0.5 \mu\text{m}$) compacts of undoped barium zirconate from nanometric starting powders only after ensuring complete conversion of carbonate to oxide, a difference in behavior that can possibly be attributed to the absence of a dopant.²¹ The microstructures obtained here for the high-temperature calcined materials (containing little residual carbonate) are similar, with grain sizes on the order of $0.4 \mu\text{m}$, to those reported in the literature for typical yttrium-doped barium zirconates prepared by a variety of routes and sintered at 1600–1700 °C.^{12,22}

3.3. Impact of Grain Growth on Proton Transport. **3.3.1. Alternating Current Impedance Spectra.** The AC impedance spectra of two representative samples are

- (19) Cervera, R. B.; Oyama, Y.; Miyoshi, S.; Kobayashi, K.; Yagi, T.; Yamaguchi, S. *Solid State Ionics* **2008**, 179(7–8), 236–242.
- (20) Rij, L.; Winnubst, L.; Jun, L.; Schoonman, J. *J. Mater. Chem.* **2000**, 10, 2515–2521.
- (21) Sin, A.; El Montaser, B.; Odier, P.; Weiss, F. *J. Am. Ceram. Soc.* **2002**, 85(8), 1928–1932.
- (22) Iguchi, F.; Yamada, T.; Sata, N.; Tsurui, T.; Yugami, H. *Solid State Ionics* **2006**, 177(26–32), 2381–2384.

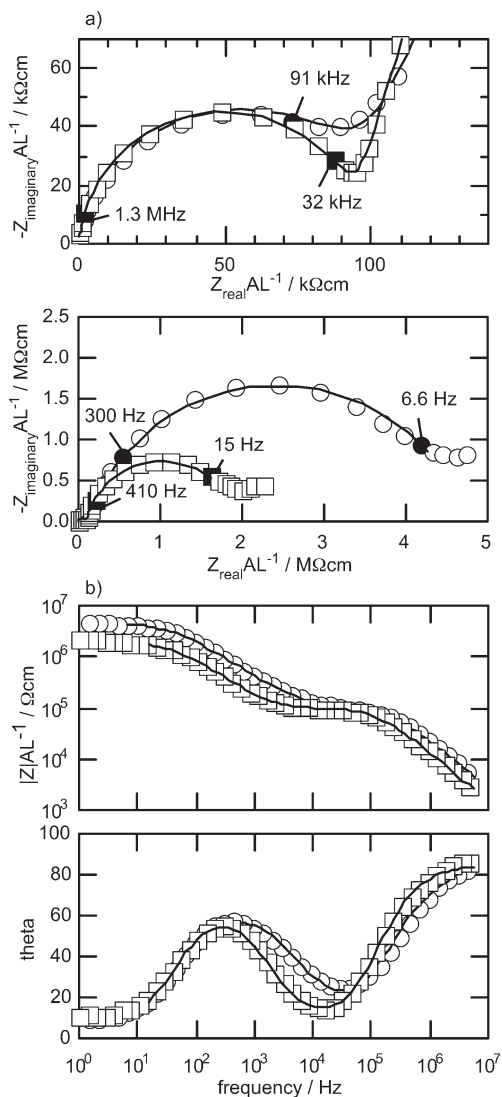


Figure 5. Impedance spectra collected at 73 °C from polycrystalline BYZ20 samples with different average distances between grain boundaries of 0.44 and 1.00 μm , presented as open circles and squares, respectively: (a) Nyquist representation (at two scales) with Z_{real} vs $Z_{\text{imaginary}}$ as parametric functions of ω , (b) Bode–Bode representation. Open symbols and solid lines represent, respectively, experimental data and fitting results obtained using an appropriate equivalent circuit.

presented in Figure 5 in both the Nyquist and Bode representations for a measurement temperature of 73 °C. The samples selected were those calcined at 1150 °C (average grain boundary spacing of 0.44 μm) and at 950 °C (average grain boundary spacing of 1.00 μm). Among the larger- and smaller-grained groups of samples, these displayed the narrowest size distribution (Figure 4). The measured composition of these two samples, determined using electron probe microanalysis, are $\text{Ba}_{0.96}\text{Zr}_{0.82}\text{Y}_{0.20}\text{O}_{3-\delta}$ and $\text{Ba}_{0.98}\text{Zr}_{0.81}\text{Y}_{0.20}\text{O}_{3-\delta}$, respectively, showing essentially equivalent composition and justifying the direct comparison. In addition, the densities are reasonably similar (90 and 99% of theoretical, respectively), and corrections for the small (9%) difference were not applied.

The high-frequency arcs of the two samples evident from the expanded scale, Figure 5a (upper figure), overlap almost completely, indicating that the grain

interior resistivities are equivalent. In contrast, the effective grain boundary resistivities, indicated by the width of the lower frequency arc (lower figure), differ substantially, with the large-grained sample displaying a resistivity that is 2.5 times smaller than that of the small-grained sample. Analysis of these impedance spectra yields the bulk (or grain interior) conductivity, the total grain boundary conductivity, the specific (or normalized) grain boundary conductivity, and the total conductivity. The results, along with literature data for similar materials, are presented in Figure 6 in Arrhenius form. Proton transport and microstructural parameters extracted from the conductivity data and the SEM images are summarized in Table 1. Characteristics of barium zirconate materials reported in the literature are summarized in Table 2 and also shown for comparative purposes in Figure 6.

3.3.2. Grain Interior Conductivities. As already indicated from the raw impedance spectra, and emphasized in the Arrhenius plot of conductivity, Figure 6a, the grain interior conductivities of the two samples are essentially identical (with a slightly, $\sim 9\%$, higher conductivity in the larger-grained sample readily attributed to the slightly higher density). The values furthermore correspond to the highest values reported in the literature.^{10,12} The activation energies for bulk proton transport obtained here, 0.46 and 0.47 eV, also correspond to literature values,^{10,12} with proton transport displaying linear behavior in the Arrhenius representation at temperatures below ~ 300 °C. The relative dielectric constants, ϵ , obtained here (99 and 155, respectively, for the small- and large-grained samples, Table 1) are somewhat larger than previously reported for barium zirconate, (46¹²) but are well within the range observed for other cubic perovskites; for example, a value of 230 has been reported for Fe-doped strontium titanate²³ at ~ 310 °C, a temperature far from the Curie point of ~ 44 K.²⁴

Because of the frequency limitations of conventional impedance meters, it is not possible to independently measure the grain interior and grain boundary conductivities at high temperatures (here, we refer explicitly to the effective grain boundary conductivity, $\sigma_{\text{eff,GB}}$, implied by the diameter of the grain boundary arc in the Nyquist impedance plot). However, the experimentally determined total conductivity can be used for extrapolating the σ_{GI} and $\sigma_{\text{eff,GB}}$ to this regime if one assumes that, despite a likely decrease in proton content due to dehydration as temperature is increased,²⁵ the ratio between the grain interior and grain boundary conductivities has an Arrhenius dependence on temperature, specifically

$$\sigma_{\text{GI}}/\sigma_{\text{eff,GB}} \propto \exp(\Delta E/k_B T) \quad (1)$$

(23) Fleig, J.; Rodewald, S.; Maier, J. *J. Appl. Phys.* **2000**, 87(5), 2372–2381.

(24) Rupprecht, G.; Bell, R. O. *Phys. Rev. A* **1964**, 135(3A), A748.

(25) Yamazaki, Y.; Babilo, P.; Haile, S. M. *Chem. Mater.* **2008**, 20(20), 6352–6357.

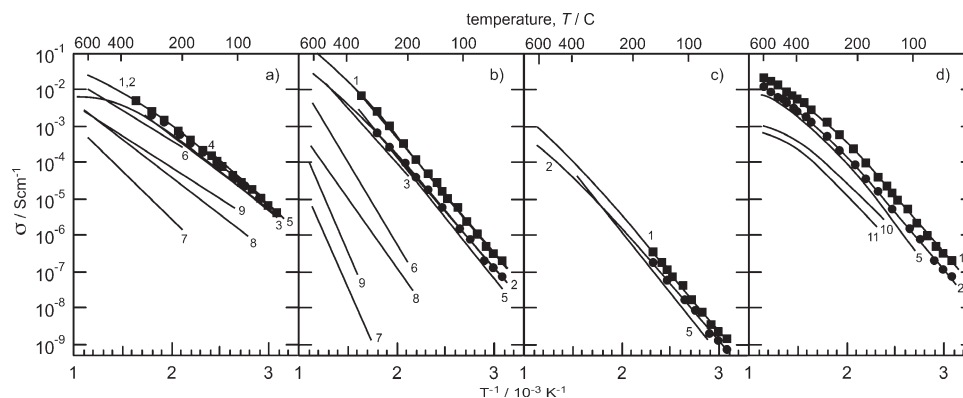


Figure 6. Temperature dependence of (a) grain interior conductivity, (b) effective (or total) grain boundary conductivity, (c) specific grain boundary conductivity, and (d) total conductivity in yttrium-doped barium zirconate. Legend information provided in Table 2. The grain interior, effective grain boundary, and specific grain boundary conductivities for the materials measured here (curves 1 and 2) are extended to higher temperatures (solid line) assuming an equivalent temperature dependence of the proton concentration in the grain and grain boundary regions and a temperature-independent ratio of bulk to grain boundary capacitance.

Table 1. Summary of Electrical and Microstructural Properties of Yttrium-Doped Barium Zirconate (as Measured Here) in Comparison to Gadolinium-Doped Barium Cerate^a

material	dopant	c_{dp} [atom %]	"grain size" [μm]	A_{GI} [SKcm ⁻¹]	H_{GI} [eV]	ϵ_{GI}	A_{GB} [SKcm ⁻¹]	H_{GB} [eV]	$\epsilon_{GB,eff}$	δ [nm]	ref
BaZrO ₃	Y	20	0.44	2.2×10^4	0.46 ± 0.01	99	3.9×10^5	0.66 ± 0.01	9.7×10^3	4.4	this work
			1.00	3.1×10^4	0.47 ± 0.01	155	1.9×10^6	0.68 ± 0.01	2.2×10^4	6.9	this work
BaCeO ₃	Gd	15	1.3	7.4×10^4	0.56	37	3.0×10^6	0.67	1.6×10^4	3.3	Haile et al. ²⁶

^a c_{dp} , dopant concentration; A , preexponential factor for proton conduction; H , activation energy for proton conduction; ϵ , relative dielectric constant; δ , grain boundary width.

Table 2. Characteristics of Yttrium-Doped Barium Zirconates Reported in Figure 6

no.	Y content [atom %]	sintering temperature [°C]	sintering time [h]	grain size [μm]	authors	ref
1	20	1600	24	1.00	this work	
2	20	1600	24	0.44	this work	
3	10	1715	30		Bohn and Schober	10
4	20	1700			Kreuer et al.	11
5	20	1600	24	0.46	Babilo et al.	12
6	5	1800	20	0.67	Iguchi et al.	22
7	5	1800	200	1.61	Iguchi et al.	22
8	10	~2200			Duval et al.	17
9	10	1720	24		Duval et al.	17
10	20	1500	20	~0.2	Cervera et al.	19
11	20	1250	10	~0.05	Cervera et al.	19

Such a relationship would be approximated if, for example, the ratio of the proton concentrations in the bulk and grain boundary regions remains constant, a plausible scenario, as discussed further below. The experimental data reveal that expression 1 is indeed obeyed in the low-temperature region in which σ_{GI} and $\sigma_{eff,GB}$ can be measured independently. The (measured) total conductivity

$$\sigma_{total}^{-1} = \sigma_{GI}^{-1} + \sigma_{eff,GB}^{-1} \quad (2)$$

can thus be used with eq 1 to obtain σ_{GI} and $\sigma_{eff,GB}$ in the high-temperature regime. The σ_{GI} so computed displays a slight downward curvature relative to linear Arrhenius behavior, a feature that has been predicted from a combination of diffusion measurements and proton solubility measurements,³ and presumably reflects the

reduction in dissolved proton content at high temperatures.²⁵

3.3.3. Total Grain Boundary Conductivities. In the absence of normalization for microstructural differences, the grain boundary conductivity of the small-grained sample, though it corresponds well to the highest in the literature for microstructurally similar material,¹² is substantially lower than that of the large-grained sample (Figure 6b). Moreover, the difference is a factor of 2.5–3.2, depending on the temperature, which corresponds closely to the difference in the mean distance between grain boundaries (= 2.3). The activation energy for proton transport in the grain boundary region is substantially larger than that in the grain interior region, ~0.67 eV as opposed to ~0.47 eV. Comparably large differences in activation energy between these regions have been previously reported in an earlier study of BYZ20¹² and in other proton conducting systems such as doped barium cerate²⁶ (Table 1).

3.3.4. Specific Grain Boundary Conductivities. The total or effective grain boundary conductivity presented in Figure 6b is a convolution of conductance across a single grain boundary and the number of grain boundaries within the sample. It is relatively common practice to extract from the impedance data the specific grain boundary conductivity (a fundamental material property independent of microstructure) by making use of the "brick layer" model.²⁶ While that model is constructed for a particular microstructural configuration (cube-shaped grains aligned with the direction of current flow), similar results can be derived for any arbitrary geometry. Specifically, ignoring grain boundaries parallel to the direction

of current flow, the total resistance, R_{total} , of a polycrystalline material is given by

$$R_{\text{total}} = \frac{\rho_{\text{GI}} L_{\text{GI}}}{A_{\text{GI}}} + \frac{\rho_{\text{GB}} L_{\text{GB}}}{A_{\text{GB}}} \quad (3)$$

where ρ is resistivity, L is length, and A is area and the subscripts GI and GB indicate grain interior and grain boundary properties, respectively. Similarly, the total capacitance, C_{total} , is given by

$$\frac{1}{C_{\text{total}}} = \frac{L_{\text{GI}}}{\epsilon_{\text{GI}} \epsilon_0 A_{\text{GI}}} + \frac{L_{\text{GB}}}{\epsilon_{\text{GB}} \epsilon_0 A_{\text{GB}}} \quad (4)$$

where ϵ and ϵ_0 are, respectively, the relative dielectric constant and the permittivity of free space.

For a material with moderate grain size, $L_{\text{GI}} \sim L_{\text{sample}}$, $A_{\text{GI}} \sim A_{\text{GB}} \sim A_{\text{sample}}$, and L_{GB} is simply the product of the grain boundary width, δ , and the number of grain boundaries, N . Furthermore, it is reasonable to take $\epsilon_{\text{GB}} \sim \epsilon_{\text{GI}}$ under the assumption that the bulk and grain boundary regions (excluding the grain boundary core discussed below) are similar in both chemistry and atomic arrangement. These approximations imply

$$\frac{R_{\text{total}} A_{\text{sample}}}{L_{\text{sample}}} = \rho_{\text{GI}} + \rho_{\text{GB}} \frac{\delta N}{L_{\text{sample}}} = \rho_{\text{GI}} + \rho_{\text{eff, GB}} \quad (5)$$

where $\rho_{\text{eff, GB}}$ is the effective or total grain boundary resistivity. The approximations also imply

$$\frac{C_{\text{GI}}}{C_{\text{GB}}} = \frac{\delta N}{L_{\text{sample}}} = \frac{\epsilon_{\text{GI}}}{\epsilon_{\text{eff, GB}}} \quad (6)$$

where, similarly, $\epsilon_{\text{eff, GB}}$ is the effective grain boundary dielectric constant. Combining (5) and (6), one obtains

$$\sigma_{\text{sp, GB}} = \sigma_{\text{eff, GB}} \left(\frac{C_{\text{GI}}}{C_{\text{GB}}} \right) \quad (7)$$

The quantity L_{sample}/N , which appears in both of these expressions, is simply equal to the grain boundary-to-grain boundary distance obtained from the mean intercept method of micrograph analysis and is moreover equivalent to the grain size of the brick layer model. Because it is the number density of grain boundaries rather than grain size that is the relevant microstructural quantity for evaluating electrical properties, no conversion from L_{sample}/N to “true” grain size is required, avoiding the introduction of uncertainties due to unknown grain geometries.²⁷ It should be noted, however, that eq 6 overestimates the grain boundary thickness because it does not account for the increased effective width of grain boundaries which are not precisely perpendicular to the direction of current flow.

From this analysis, we obtain grain boundary thicknesses of 4.4 and 6.9 nm, respectively, for the

small-grained and large-grained samples. These values are comparable to those reported previously for barium cerate,²⁶ although in the previous work, the grain boundary thicknesses for samples with differing grain sizes were essentially identical. A possible explanation for the behavior observed here (that of slightly different grain boundary thicknesses between samples) is discussed below. In addition to wider grain boundaries, the large-grained sample displays a greater specific grain boundary conductivity than the small-grained sample, by a factor of 1.8–1.9. The combination of higher specific grain boundary conductivity and greater grain boundary thickness essentially compensates to yield materials with similar resistance values per grain boundary, that is, $(\delta_2/\delta_1)(\sigma_{\text{GB},1}^{\text{sp}}/\sigma_{\text{GB},2}^{\text{sp}}) \approx 1$, where subscripts 1 and 2 refer to the two different samples. Thus, the observed increase in total (or effective) grain boundary conductivity in the large-grained material relative to the small-grained one is primarily due to the decrease in the number density of grain boundaries (rather than differences in the properties of the individual grain boundaries).

3.3.5. Total Conductivities. As implied by eq 2, the total conductivity of the electrolyte (Figure 6d), which is the relevant quantity for any technological application, is dominated by the least conductive component in the system. Accordingly, at low temperatures, at which the grain boundary conductivity is low for both samples, the total conductivity essentially tracks the total grain boundary conductivity and is substantially higher for the large-grained material than the small-grained analog. At higher temperatures, as the grain boundary conductivity increases in accordance with the high activation energy, the bulk becomes a more important factor. For the small-grained sample, the total conductivity at temperatures above ~ 450 °C is colimited by both the grain boundary and bulk resistance. Even at a temperature of 600 °C, the total conductivity does not reach the computed (extrapolated) value of the bulk conductivity. In contrast, in the case of the large-grained sample, the total conductivity at temperatures above ~ 450 °C is almost entirely due to grain interior characteristics, as indicated by the close match between the total conductivity and the extrapolated value of the high-temperature grain interior conductivity. Thus, further increases in grain size would be expected to provide only marginal increases in the total conductivity.

A more quantitative evaluation of the impact of grain size on the total proton conductivity in these materials is possible by examining the ratio of the total conductivity to the computed, high-temperature grain-interior conductivity, Figure 7. This ratio, ranging from 0 for a sample that is entirely grain-boundary-dominated to unity for a sample that is entirely grain-interior-dominated, provides a measure of the reduction in the total conductivity due to high grain boundary resistance. In accord with the high activation energy for grain boundary conductivity, the ratio approaches unity at a high temperature for both samples; however, it is much larger for the large-grained material than the

(26) Haile, S. M.; West, D. L.; Campbell, J. J. *Mater. Res.* **1998**, *13*(6), 1576–1595.

(27) Han, J. H.; Kim, D. Y. *Acta Met. Mater.* **1995**, *43*, 3185–3188.

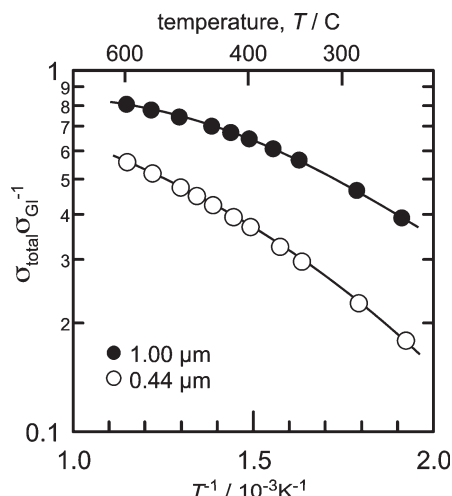


Figure 7. Impact of grain size on total conductivity in polycrystalline BYZ20. The ratio (y axis), ranging from 0 for a sample that is entirely grain-boundary-dominated to unity for a sample that is entirely grain-interior-dominated, provides a measure of the reduction in the total conductivity due to high grain boundary resistance.

small-grained material. Indeed, in the intermediate temperature range of relevance for SOFC operation (400–600 °C), the ratio in the small-grained sample ranges from 0.37 to 0.56, indicating that the total conductivity has reached only 56% of the possible grain interior conductivity even at 600 °C. In contrast, the total conductivity of the large-grained material reaches ~70% of the grain interior at a temperature of only 450 °C.

The overall consequence of the preparation of large-grained BYZ20 is an electrolyte material with a total conductivity at 450 °C of greater than $1 \times 10^{-2} \text{ Scm}^{-1}$, a stated target value for fuel cell applications with a 15- μm -thick electrolyte.¹ In fact, the total conductivity of the large-grained BYZ20 exceeds that of samarium-doped ceria²⁸ in the entire targeted intermediate temperature range. Thus, the factor of ~3 enhancement in total conductivity achieved here (relative to the highest values previously reported in the literature), combined with the relative simplicity of the synthesis procedures outlined here, opens up new opportunities for utilizing doped barium zirconate in electrochemical applications. Specifically, at moderate temperatures, inexpensive interconnect components can be utilized, and at moderate film thicknesses, high electrical potential gradients across the electrolyte are avoided.

4. Conclusions

A fabrication protocol based on chemical solution synthesis of precursor materials and subsequent reactive sintering for obtaining large-grained $\text{BaZr}_{0.8}\text{Y}_{0.2}\text{O}_{3-\delta}$ (BYZ20) has been developed. A combination of incom-

plete calcination, such that some amount of barium carbonate remains prior to sintering, and nanometric powders of the perovskite phase appears to be necessary for enhanced grain growth. Desirable powder characteristics could be achieved by limiting calcination temperatures to 1050 °C or lower, at which the residual barium carbonate content was 8 wt % or higher. When such a procedure is used (with a calcination temperature of 850 °C and a sintering temperature of 1600 °C), a mean distance between grain boundaries as large as 1.4 μm could be achieved, while also attaining a relative density as high as 97%. The impact of large grain size on the total conductivity was found, as expected, to be extremely significant. A comparison of samples with grain sizes differing by a factor of ~2.3 showed a difference in effective grain boundary conductivity by an almost identical factor of 2.5–3.2, depending on the temperature. Unexpectedly, the inherent properties of the two samples were found to be different, with the larger-grained sample displaying a slightly larger specific grain boundary conductivity but also slightly larger grain boundary width. Together, these factors combine to create grain boundaries with impedance characteristics on a per boundary basis that are similar between the two samples. Thus, the enhancement of the effective grain boundary conductivity (and accordingly to that of the total conductivity) is almost entirely due to the smaller number density of grain boundaries. As with many other ceramic ionic conductors, the grain boundaries displayed a higher activation energy for ion transport than the bulk, as a consequence of which grain boundaries have diminishing impact on the total conductivity as the temperature is increased. The total conductivity of the small-grained material reached only 56% of the grain interior value at 600 °C, indicating that even at this high temperature the grain boundaries remain detrimental. In contrast, the total conductivity of the large-grained material reached ~70% of that of the grain interior at a temperature of only 450 °C. The total conductivity attained at this temperature, $1 \times 10^{-2} \text{ Scm}^{-1}$, is competitive for electrochemical and especially fuel cell applications. Further increases in grain size (beyond a mean boundary-to-boundary distance of ~1 μm) would be expected to provide only marginal increases in the total conductivity.

Acknowledgment. This work was supported by the Gordon and Betty Moore Foundation and by JSPS Postdoctoral Fellowships for Research Abroad.

Note Added after ASAP Publication. Due to a production error, the footnote for Table 1 was in inadvertently deleted from the article in the version of this paper published ASAP May 20, 2009; the corrected version published ASAP June 12, 2009.

(28) Lai, W.; Haile, S. M. *J. Am. Ceram. Soc.* **2005**, 88(11), 2979–2997.